

## POLARIMETRY TOWARD THE *IRAS* VELA SHELL. I. THE CATALOG

A. PEREYRA<sup>1</sup> AND A. M. MAGALHÃES<sup>2</sup>

Instituto de Astronomia, Geofísica e Ciências Atmosféricas, Universidade de São Paulo, Caixa Postal 3386,  
São Paulo, SP 01060-970, Brazil; antonio@iagusp.usp.br, mario@iagusp.usp.br

Received 2001 September 26; accepted 2002 March 28

### ABSTRACT

We have obtained linear polarization measurements of stars along the western side of the *IRAS* Vela Shell toward HD 62542. From 16 CCD fields distributed along the ionization front (I-front) we have built a catalog of 856 objects with polarization signal-to-noise ratio larger than 10. We detect very significant levels of polarization and hence an appreciable magnetic field throughout the region. Composite polarization maps around the I-front are shown. In some regions the polarization vectors are parallel to the I-front, but a perpendicular trend is also evident along parts of the front. In addition, the polarization pattern seems to be affected by gas streaming inside the cloud.

*Subject headings:* catalogs — ISM: clouds — ISM: individual (Gum Nebula, Vela Shell) —  
ISM: magnetic fields — polarization — stars: individual (HD 62542)

*On-line material:* additional figures, machine-readable table

### 1. INTRODUCTION

Interstellar shells and associated shock waves and ionization fronts may be driven by supernova explosions, pressure of photoionized gas, stellar winds, and collisions between fast-moving clumps of interstellar gas (Draine & McKee 1993). The interaction between expanding shells and magnetic field was examined by Troland & Heiles (1982) using Zeeman measurements, and they concluded that the magnetic field severely limits the density enhancement in the cool, postshock gas. This is indeed expected theoretically (Spitzer 1978). It is clear that magnetic fields in ionization fronts and shocks may be important in the evolution of these systems. Magnetic ionization fronts have been modeled for parallel (Redman et al. 1998) and oblique (Williams, Dyson, & Hartquist 2000) magnetic fields. In the same way, the structure of shocks in a weakly ionized and dustless media depends on the orientation of the magnetic field with respect to the velocity of the shock (Hartquist, Pilipp, & Havnes 1997; Pilipp, Hartquist, & Havnes 1990; Pilipp & Hartquist 1994; Wardle 1998).

Polarization maps of background stars shining through obscured regions may reveal the magnetic field structure of the regions (for reviews see Jones 1996; Lazarian 2000). The direction of the linear polarization will provide the direction of the magnetic field projected on the plane of the sky in the classical paramagnetic relaxation alignment (Davis & Greenstein 1951; Jones & Spitzer 1967), where the average grain profile is oriented perpendicular to the magnetic field. This is generally not disputed when the visual absorption is not too high (Lazarian, Goodman, & Myers 1997). Other alignment mechanisms, however, may predict grain alignment parallel to the field, such as those involving supersonic flows (Lazarian 1994).

The interstellar medium (ISM) toward the Puppis-Vela region shows important, large-scale structures within 1–2 kpc from the Sun. Sahu (1992) analyzed the morphology and kinematics of the ISM in Puppis-Vela ( $l = 240^\circ$ ,  $-275^\circ$ ,  $|b| < 20^\circ$ ) and identified three main structures, in order of decreasing distance from the Sun: the Vela Molecular Ridge ( $r \sim 1$  kpc), the Gum Nebula (GN,  $r \sim 800$  pc), and the *IRAS* Vela Shell (IVS,  $r \sim 450$  pc). Also present are OB and R associations (Vela OB1, Vela OB2, and Vela R2). Early-type stars include  $\zeta$  Puppis (O5 Iaf), the brightest O star in the sky, and  $\gamma^2$  Velorum (WC8+O9I), the brightest and probably the nearest Wolf-Rayet binary. A great number of cometary globules and dark clouds are distributed in the region (Hawarden & Brand 1976; Sandqvist 1976; Zealey et al. 1983; Reipurth 1983).

The Vela Molecular Ridge is a giant molecular cloud that sits behind both the GN and the IVS. In turn, the GN is an enormous structure of H $\alpha$  emission with an angular diameter of  $\sim 36^\circ$  ( $\sim 500$  pc), occupying a great part of Puppis and Vela. Reynolds (1976a, 1976b) proposed that the GN is an old supernova remnant heated by the ionizing UV flux from  $\zeta$  Puppis and  $\gamma^2$  Velorum.

Sahu (1992), based on *IRAS* maps of extended emission and kinematic studies of the ionized gas in Puppis-Vela and proper motions in Vela OB2, discovered the existence of the IVS, a ringlike structure with sections previously mistaken as part of the GN but much closer. The IVS has a radius of  $\sim 7.5^\circ$  ( $\sim 60$  pc) and is positioned asymmetrically ( $l, b \sim (263^\circ, -7^\circ)$ ) with respect to the GN center. While  $\zeta$  Puppis, a runaway from the Vela R2 association, is indeed primarily responsible for the ionization of the GN, the Vela OB2 association, which includes  $\gamma^2$  Velorum, is responsible for the formation of the IVS through stellar winds and radiation pressure. The position of the IVS on the sky is shown in Figure 1. A more detailed, 100  $\mu\text{m}$  view is shown in Figure 2.

The IVS is interesting for other reasons. The line of sight to HD 62542 intercepts the west side of the IVS (Figs. 2 and 3). HD 62542 has a rather anomalous UV extinction curve (Cardelli & Savage 1988) with a very weak 2200 Å extinction bump. Previous works associated the structure toward

<sup>1</sup> Also at Facultad de Ciencias, Universidad Nacional de Ingeniería, Av. Túpac Amaru 210, Rímac, Casilla 31-139, Lima, Perú.

<sup>2</sup> Visiting Astronomer, Cerro Tololo Inter-American Observatory. CTIO is operated by AURA, Inc., under contract to the National Science Foundation.

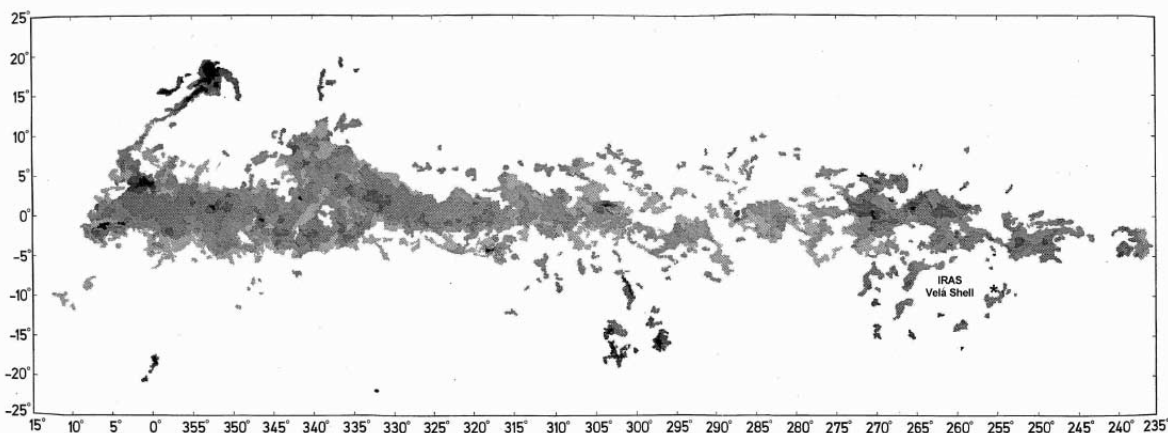


FIG. 1.—Galactic distribution map of dark clouds from Feitzinger & Stüve (1984) with the *IRAS* Vela Shell region indicated. The position of HD 62542 is shown by the asterisk (\*).

HD 62542 with the GN (Cardelli & Savage 1988), but its spatial distribution is in fact more consistent with that of the IVS (Sahu 1992; Churchwell et al. 1996). The east border of the structure (inside the cavity) shows a well-defined ionization front (I-front), seen almost edge-on, with different curvatures in the north and south sections. The IVS far-infrared dust emission accompanies the morphology of the I-front (Sahu 1992), implying that the radiation field of Vela OB2 and shocks induced by the expansion of the shell must heat the dust. A scenario of an ionization and shock front (I/S-front) might prevail in this region (Churchwell et al. 1996). Whittet et al. (1993) analyzed the *IRAS* sources around HD 62542 and concluded that there is no evidence for current or recent star formation along that ridge (Fig. 3).

Churchwell et al. (1996) studied this region in CS, and this emission accompanies the I/S-front and the emission from dust. They found that the kinetic energy of the CS cloud is 1 order of magnitude higher than the gravitational potential energy. This indicates that the structure is not gravitationally bound and would disperse on very short timescales were it not for the ram pressure of the expanding IVS, which continually sweeps up new interstellar matter into the cloud.

In summary, the *IRAS* Vela Shell encloses a cavity that appears to have been formed by stars of the Vela OB2 association through the effects of stellar winds and supernovae explosions (Sahu 1992). In this paper we present a catalog of the linear polarization of stars seen toward a western section of the *IRAS* Vela Shell. Our technique provides good quality data for a relatively large number of objects. We also discuss the general properties of the polarization vectors throughout the region. The fact that the structure is seen almost edge-on is indeed helpful to the interpretation of polarization measurements. In a forthcoming paper, we present a fuller analysis of the data and relate them to other existing data on the IVS structure.

## 2. OBSERVATIONS AND DATA REDUCTION

The observations were made using a CCD imaging polarimeter (Magalhães et al. 1996) attached to the 1.5 m Telescope of Cerro Tololo Inter-American Observatory

(CTIO), Chile. The polarimeter is a modification of the CTIO direct CCD camera to allow for high precision imaging polarimetry. The first element in the beam is a rotatable, achromatic half-wave retarder followed by a Savart plate. This provides two images of each object in the field, separated by 1 mm (corresponding to about 18'' at that telescope's focal plane) and with orthogonal polarizations. One polarization modulation cycle is covered for every 90° rotation of the waveplate. The simultaneous imaging of the two beams allows observing under nonphotometric conditions and at the same time the sky polarization is practically canceled (Magalhães et al. 1996).

Figure 3 shows the distribution of CCD fields observed and Table 1 provides the position of the field centers. The data were collected in 1991 December and 1992 December. CCD exposures for each field were taken through the *V* filter with the waveplate rotated through four positions 22.5° apart. With the 1024 × 1024 CCD used (CTIO Tek No. 1),

TABLE 1  
CCD FIELD POSITIONS

Field	R.A. (J2000)	Decl. (J2000)	Mission
01.....	7 42 37.08	-42 13 44.66	91
02.....	7 42 01.22	-42 07 02.30	91
03.....	7 41 25.31	-42 02 02.93	91
04.....	7 43 12.93	-42 20 25.03	91
05.....	7 38 59.84	-41 36 55.29	92
06.....	7 39 32.15	-41 28 59.42	92
07.....	7 40 03.96	-41 36 59.53	92
08.....	7 40 03.70	-41 44 59.52	92
09.....	7 40 35.51	-41 53 01.63	92
10.....	7 42 11.43	-42 01 06.96	92
11.....	7 42 10.92	-42 17 07.95	92
12.....	7 42 42.72	-42 25 11.05	92
13.....	7 42 10.66	-42 25 07.94	92
14.....	7 41 06.41	-42 29 03.71	92
15.....	7 40 09.39	-42 56 59.98	92
16.....	7 39 36.94	-43 08 58.84	92

NOTE.—Units of right ascension are hours, minutes, and seconds, and units of declination are degrees, arcminutes, and arcseconds.

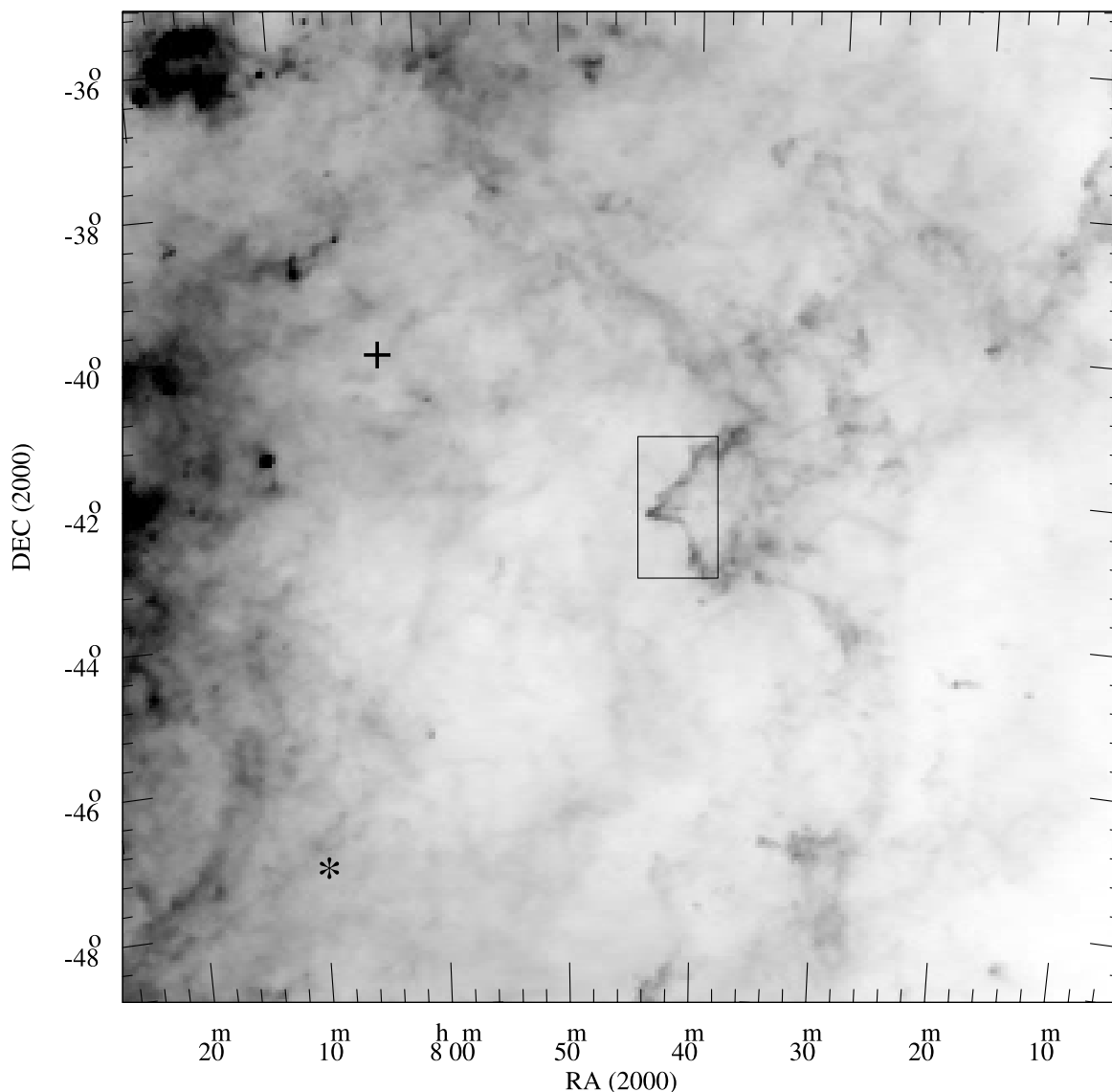


FIG. 2.—*IRAS* image in  $100\ \mu\text{m}$  of the west section of the *IRAS* Vela Shell toward HD 62542, obtained from the Sky View Web page (<http://skyview.gsfc.nasa.gov/skyview.html>). The figure covers  $14^\circ \times 14^\circ$ . The  $\sim 1^\circ \times 2^\circ$  boxed region indicated highlights the section of the IVS which we studied and which is detailed in Fig. 3.  $\zeta$  Puppis and  $\gamma$  Velorum are indicated by a plus and an asterisk (\*), respectively.

each field covers  $\sim 8' \times 8'$ . The exposure time at each position was typically 300 s. Exceptions are fields 01 (10 s), 02 (180 s), 03 (240 s), and 04 (240 s).

After bias and flat field corrections, photometry was performed for both images of stars in each field using the IRAF<sup>3</sup> DAOPHOT package, a group of procedures which create a set of data files for each image field. A special purpose FORTRAN routine processed these data files and calculated the normalized linear polarization from a least-squares solution. This yields the percent linear polarization ( $P$ ), the polarization angle ( $\theta$ , measured from north to east), the Stokes parameters  $Q$  and  $U$ , as well as the theoretical (i.e., the photon noise) and measured ( $\sigma_P$ ) errors. The latter are obtained from the residuals of the observations at each

waveplate position angle ( $\psi_i$ ) with respect to the expected  $\cos 4\psi_i$  curve and are quoted in Table 2; they are consistent with the photon noise errors (Magalhães, Benedetti, & Roland 1984). A set of specially developed IRAF tasks to study the polarization data in (eventually crowded) stellar fields (Pereyra 2000, PCCDPACK package) was extensively used. Each field was painstakingly checked for objects with suspicious polarization that were usually related to an overlapping image of a nearby object; these objects were removed from the compilation presented here.

The instrumental  $Q$ - and  $U$ -values were converted to the equatorial system from standard star data obtained in the same night. The instrumental polarization was measured to be less than 0.03%, and no such correction was applied. We have not purposely applied any correction for statistical bias (Simmons & Stewart 1985) to the polarization values in Table 2, so that others may handle the data more readily. Such correction would be small in any case for the high  $P/\sigma_P$ -values (§ 4) of the catalog.

<sup>3</sup> IRAF is distributed by the National Optical Astronomy Observatory, which are operated by the Association of Universities for Research in Astronomy, Inc., under cooperative agreement with the National Science Foundation.

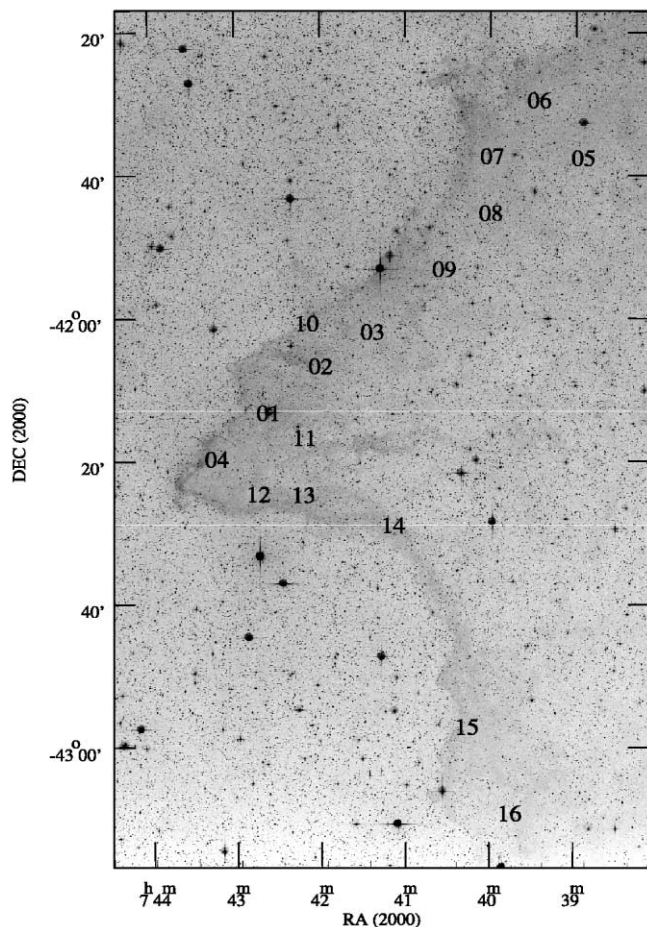


FIG. 3.—Region of the *IRAS* Vela Shell toward HD 62542 over which we have performed the imaging polarimetry. The underlying images in this and the remaining figures are from the Digitized Sky Survey and were obtained either through the Sky View Web page (Fig. 15) or its CD-ROM (this figure and Figs. 5 through 14). The region covers an area of  $\sim 1^\circ \times 2^\circ$ . The numbers indicate the positions of each one of the 16 CCD fields observed. Each field covers an area of  $8' \times 8'$ . The position of HD 62542 coincides with that of the center of field 01.

### 3. THE CATALOG

The polarimetric data are presented in one long table with the data of the 16 CCD fields (Table 2) and the associated finding charts (Figs. 15a–15p, available in the on-line edition of the *Astrophysical Journal Supplement*), one for each

CCD field. The underlying images in the finding charts were made from the Digitized Sky Survey (DSS). In Table 2, the first column is the CCD field number. The second column is the identification number (ID) of the object in each field. This number labels the position of the object in the finding charts. The fourth and fifth columns are the equatorial coordinates (2000). The estimated error in the position is less than  $1''$ . The sixth and seventh columns are the polarization value in the *V* filter and its error. The polarization angle is in the eighth column and the estimated visual magnitude (see below) is in the last column.

The positions of the objects were calculated by comparing objects present in both our CCD fields and the DSS. In this way the  $(x, y)$  positions in pixels were transformed to (R.A., decl.) coordinates using the plate parameters available in the digitized image headers. The images used for this conversion are the same used as finding charts for each field.

For a given field the visual magnitudes were calculated using the first of the four images obtained, each corresponding to a given half-waveplate position. For a given object we added the counts of the ordinary and extraordinary beams within the aperture used in the calculation of the polarization for the object. The instrumental magnitude obtained was then corrected to the standard system. The additive correction was estimated in each field by obtaining an average difference between the values of the magnitudes of the General Star Catalog (Lasker et al. 1990) (GSC) and our instrumental magnitudes for objects present in both samples. The GSC magnitudes used in this correction correspond to that of a Schmidt plate with the combination emulsion/filter = IIIaJ/GG395, centered in  $4500 \text{ \AA}$  (Lasker et al. 1990) and which were transformed to the *V* filter by Lasker et al. (1990). These magnitude estimates must be taken just as indicative because of the impossibility of obtaining appropriate corrections to our data for the color term and the extinction coefficient as usual. The typical magnitude uncertainty in our catalog is dominated by the uncertainty in the GSC magnitudes and was estimated to be 0.33 mag from the resulting rms deviations. A histogram of the calculated magnitudes is shown in Figure 4.

### 4. POLARIZATION MAPS

In Figure 5 we show a mosaic of the polarization maps across the  $\sim 1^\circ \times 2^\circ$  region studied. In the figure each vector represents an object with polarization signal-to-noise ratio,  $P/\sigma_P$ , larger than 10. As mentioned earlier, data with a

TABLE 2  
FIELD DATA

Field	ID	Flag	R.A. (J2000.0)	Decl. (J2000.0)	$P_V$ (%)	$\sigma_{P_V}$ (%)	$\theta$ (deg)	$V$ (mag)
01.....	9	7	7 42 16.21	-42 11 43.30	0.309	0.019	81.9	15.74
01.....	23	7	7 42 20.26	-42 11 17.44	0.344	0.029	29.5	15.01
01.....	24	7	7 42 21.96	-42 15 43.07	2.088	0.127	122.4	17.04
01.....	30	7	7 42 23.86	-42 10 08.11	0.981	0.013	45	14.17
01.....	32	7	7 42 24.56	-42 11 24.34	1.948	0.066	62.6	16.42

NOTES.—Units of right ascension are hours, minutes, and seconds, and units of declination are degrees, arcminutes, and arcseconds. Table 2 is available in its entirety in the electronic edition of the *Astrophysical Journal Supplement*. A portion is shown here for guidance regarding its form and content.

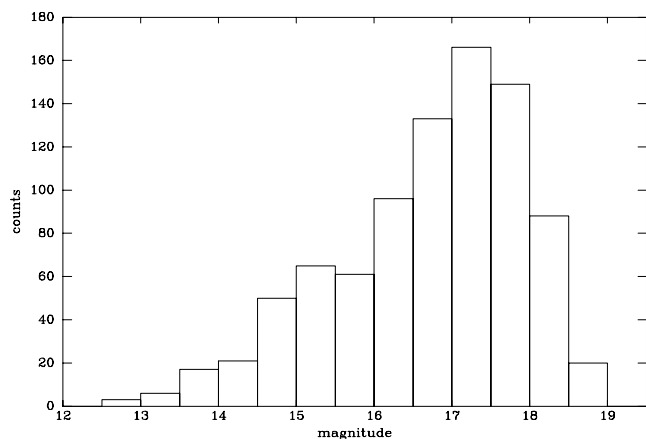


FIG. 4.—Histogram of magnitudes for the objects in the catalog

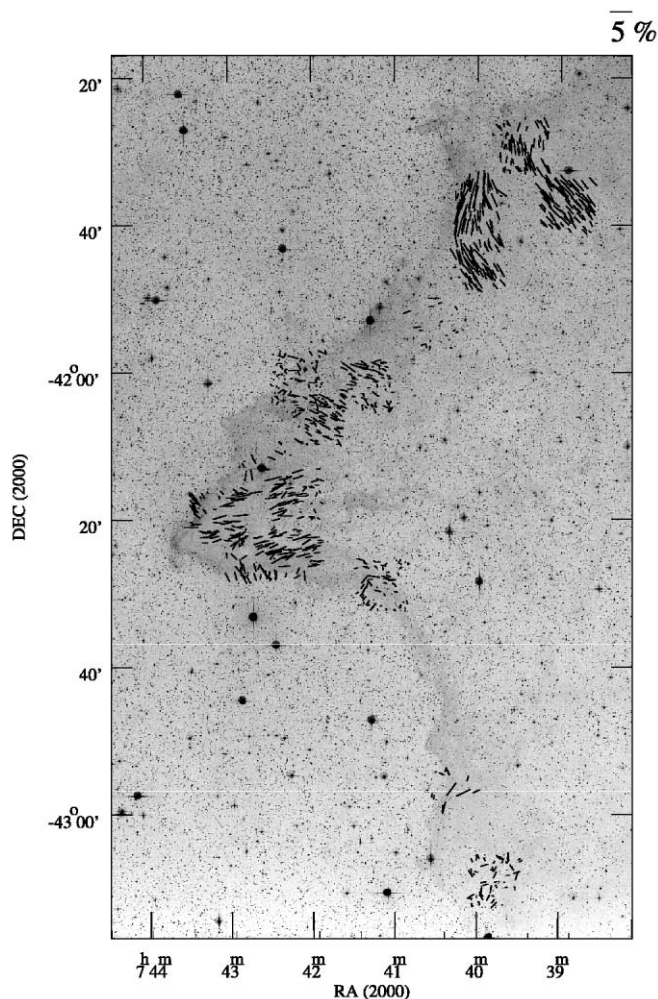
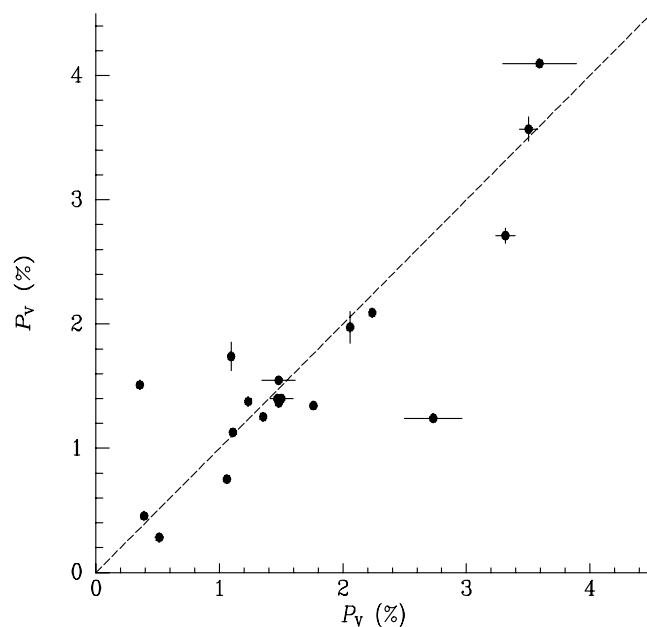


FIG. 5.—Mosaic of the polarization vector maps for the 16 CCD fields superimposed on a Digitized Sky Survey image. The polarization scale is shown at the top of the figure. Each vector represents an object with polarization signal-to-noise ratio larger than 10. The total number of objects in the catalog and plotted above is 856.

lower S/N ratio may still be useful but less certain especially for faint objects where overlapping with the ordinary or extraordinary beams of nearby objects may occur. The total number of objects with  $P/\sigma_P > 10$  is 856.

Nineteen objects have two independent polarimetric measurements from overlapping fields and are indicated with the flag in the third column and in footnotes of Table 2. A plot of these measurements is shown in Figure 6, where it can be seen that they are reasonably consistent with one another. The weighted mean value of the differences between the pairs of polarization measurements is  $0.24\% \pm 0.01\%$ , comparable with the typical error in the catalog,  $\sim 0.1\%$ , multiplied by  $\sqrt{2}$ . For the polarization angles, the weighted mean value of the differences is  $5^\circ.2 \pm 0^\circ.1$ . A typical polarization value in the catalog is  $\sim 1\%$  which, with the typical error above, gives  $\sim 3^\circ$  as a typical uncertainty for the position angle, again comparable to the weighted mean value of the position angle differences. Of course, polarization, being a positive definite quantity, does not obey normal statistics, as opposed to  $(Q, U)$  values with a good polarimetric signal-to-noise (Simmons & Stewart 1985). Using the  $(Q, U)$  values for the pairs of polarization measurements of Figure 6 we obtain similar results. In any case, any averaging of polarization data for stars in the catalog by users should be done using  $(Q, U)$  values.

From a cursory comparison between the observed alignment and the morphology of this section of the IVS, it is evident from Figure 5 that more than one alignment structure of the polarization vectors along the I/S-front prevails. To show this in more detail, we present sections of the composite polarization map by grouping two or three fields superimposed on their respective DSS images. In this preliminary analysis, we follow the ridge roughly from north to south and concentrate on the qualitative patterns of the polarization maps. Some fields are shown more than once to help follow the patterns along the front from one figure to the next.

FIG. 6.—Objects with two independent polarimetric measurements with errors. The dashed line is just the  $45^\circ$  line to help the comparison.

## 4.1. Comments on Individual Regions

## 4.1.1. Fields 05, 06, and 07

In Figure 7 we show the polarization map of fields 05, 06, and 07. The area shown is  $25' \times 18'$  ( $3.3 \times 2.4$  pc, at 450 pc). A very smooth structure of the polarization vectors is evident within each CCD field and from one CCD field to the other. It is also interesting to note the apparent alignment of the polarization pattern with the overall morphology of the I/S-front. The pattern of field 07 in particular, closer to the ridge at that point in the

nebula, follows closely that of the nebula border. Field 07 also shows higher polarization values than either fields 05 or 06; given the otherwise very smooth inferred magnetic field structure across the area, this is probably related to the variation of inclination of the magnetic field to the line of sight from one field to the other. Another possibility is that of field enhancement in the compressed postshock gas. This might translate into a smaller dispersion of position angles for field 05 as compared with that of field 07. Such analysis will be made in the forthcoming paper.

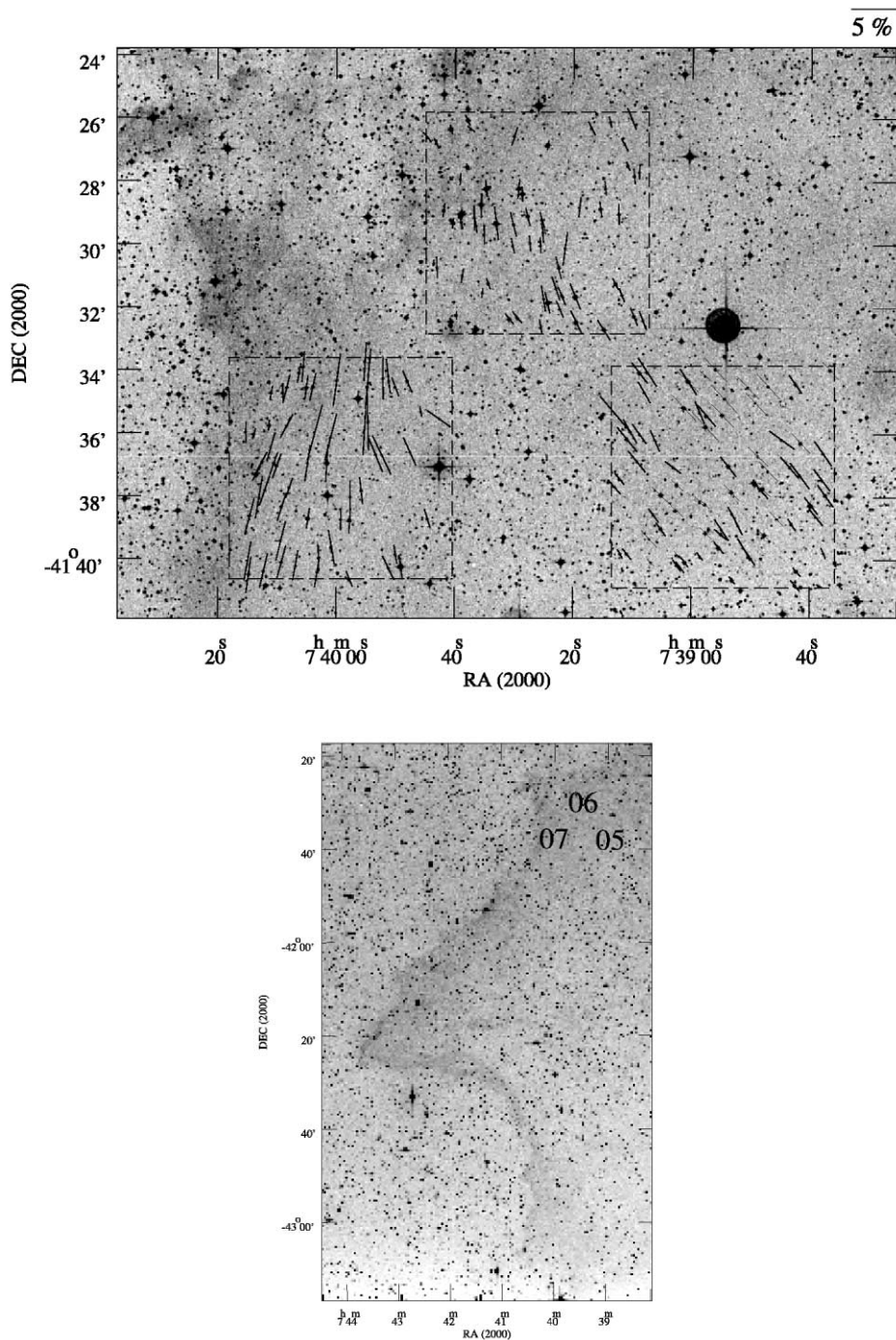


FIG. 7.—Polarization vector map for fields 05, 06, and 07. The area covered by each field is outlined by a dashed box. The positions of the individual fields are shown in the smaller frame for clarity. The percent polarization scale is shown at the top of the figure. The scales for each of the remaining figures are similarly shown.

4.1.2. *Fields 07, 08, and 09*

In Figure 8 we show the vector plots for fields 07, 08, and 09, spread over an area of  $18' \times 30'$  ( $2.4 \times 3.9$  pc). The observed polarization pattern of field 07 follows the border of the nebular ridge and seems to join smoothly with that of field 08 to the south. In field 09 the polarization values are low and no dominating pattern is evident. Field 09 covers an emission structure which is seen separated from the more northern section of the ridge where fields 07 and 08 sit.

4.1.3. *Fields 10 and 11*

Fields 10 and 11 are shown in Figure 9. The area shown is  $12' \times 28'$  ( $1.6 \times 3.7$  pc). The saturated star near field 11 is HD 62542. Like field 09 to its northwest, field 10 does not show a clear polarization pattern. We note that field 10 straddles both sides of the well-defined interface of the ridge. The emission is also not uniform over the field. Field 11 is farther from the borders of the ridge and is also immersed in a cirrus-like emission that the polarization pattern appears to follow. This field is situated *downstream* of field 04 and clump A of Churchwell et al. (1996); see § 4.1.5 below. The polarization pattern of field 11 may well be

following the polarization pattern displayed by the denser parts of field 04 (see Fig. 5).

4.1.4. *Fields 02 and 03*

In Figure 10 we show the composite polarization map for the fields 02 and 03. The area shown covers  $18' \times 15'$  ( $2.4 \times 2.0$  pc). Both fields are inside the emission region and a pattern almost perpendicular to the ridge prevails. Nevertheless, small distortions in this pattern exist and may be correlated with the uneven observed emission. In addition, almost directly east of field 02 (SE of field 03), Churchwell et al. (1996) detected a condensation in CS emission (their clump C) which seems, in their own words, to be “eroding away” due to the expanding nebula. It is possible that the polarization pattern in field 02 is just reflecting this swept-up gas. See also discussion on field 04 below and § 4.2.

4.1.5. *Fields 01 and 04*

Figure 11 shows fields 01 and 04 in an area which covers  $16' \times 16'$  ( $2.1 \times 2.1$  pc). Field 01, centered in HD 62542 (the saturated star in the DSS image), shows few objects with a polarization S/N ratio larger than 10, since only an 10 s integration time per half-waveplate position was used. No

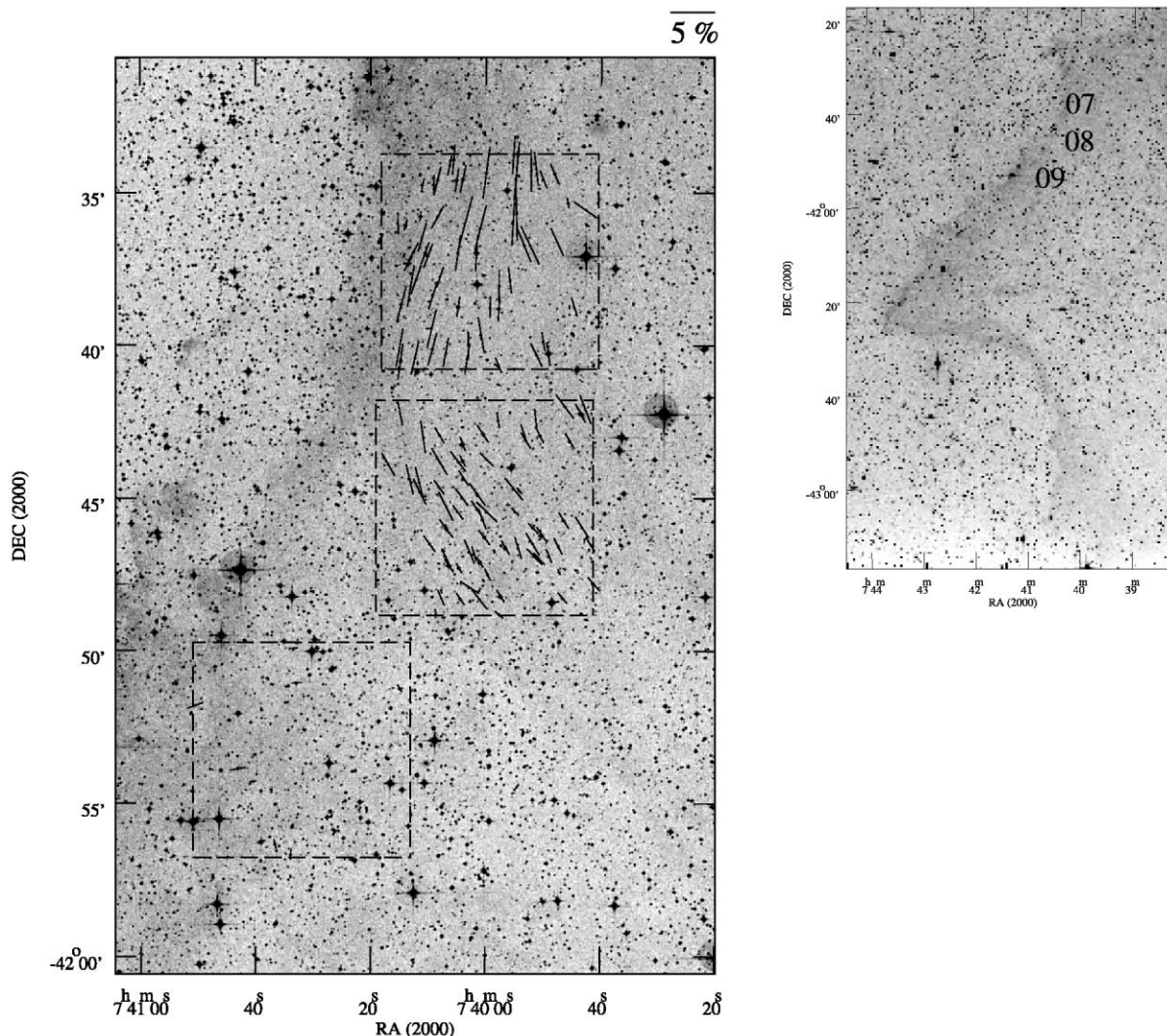


FIG. 8.—Polarization vector map for fields 07, 08, and 09

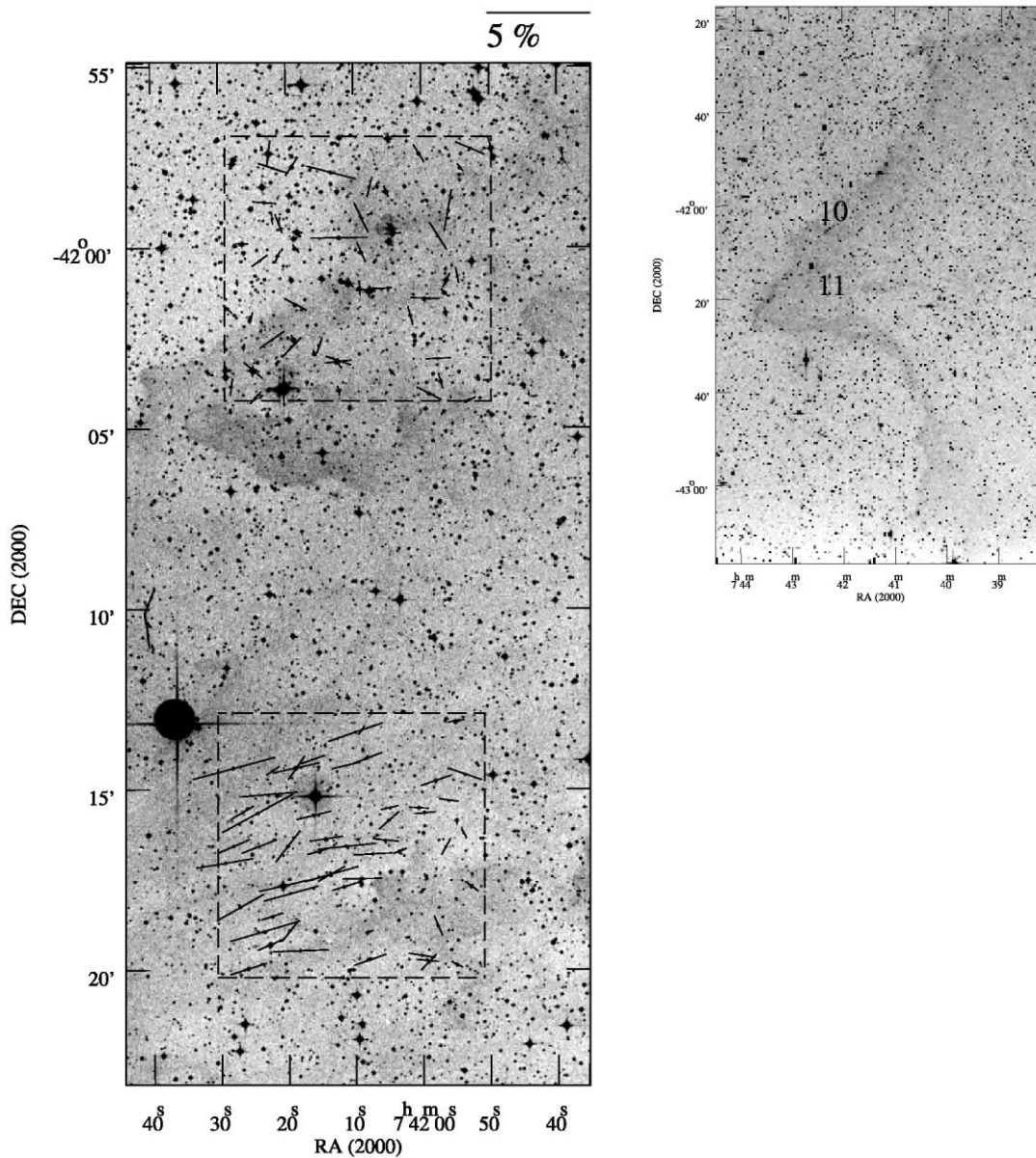


FIG. 9.—Polarization vector map for fields 10 and 11

general alignment pattern seems evident. Nevertheless, a careful examination shows that objects near HD 62542 (ID 23, 73, 76, and 88 in field 01 of Table 2) present values of polarization position angle similar to the star (Clayton et al. 1992, 30°:8).

In field 04, a bimodal alignment pattern exists: one at  $\sim 40^\circ$  just east of the ridge and another pattern at  $\sim 100^\circ$  toward the denser parts of the nebula. This symmetry resembles that of field 12 discussed in § 4.1.6 below (Fig. 12). It may not be totally unexpected that the denser parts of field 04 show neither a perpendicular nor a parallel alignment with the nearby ridge since the latter changes concavity around that region, in addition to the effects of a projection of a three-dimensional surface on the sky. It is, however, also of interest to note that the region southeast of field 04 is coincident with the condensation labeled V12 in the list of Vilas-Boas, Myers, & Fuller (1994) and clump A in the CS study of Churchwell et al. (1996). The latter authors suggest that the CS emission around the clump may

be swept-up ambient gas by the ram pressure of the expanding nebula. Interestingly, the field lines of field 04, pointing away from the condensation, would seem to be consistent with such picture.

#### 4.1.6. Fields 11, 12, and 13

The composite polarization map of fields 11, 12, and 13 is shown in Figure 12. The area shown in this figure covers  $20' \times 20'$  ( $2.6 \times 2.6$  pc). In field 11, as pointed out above, the polarization pattern seems to follow the cirrus-like structures seen in emission. The polarization patterns of fields 12 and 13 seem to smoothly join that of field 11. The pattern of field 12 is very interesting and similar in some respects to that of field 04. Northwest of field 12 center, the pattern follows  $\theta \sim 115^\circ$  like fields 11 and 13. Northeast the field center, another polarization direction seems to prevail. South of the field center, a pattern perpendicular to the southern ridge is observed. Field 12 includes clump B of Churchwell et al. (1996),

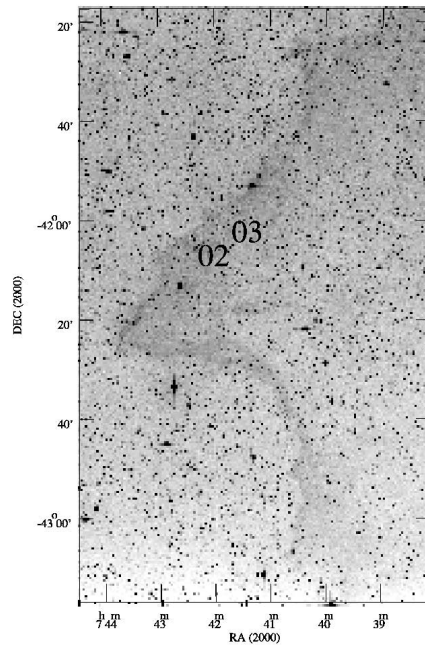
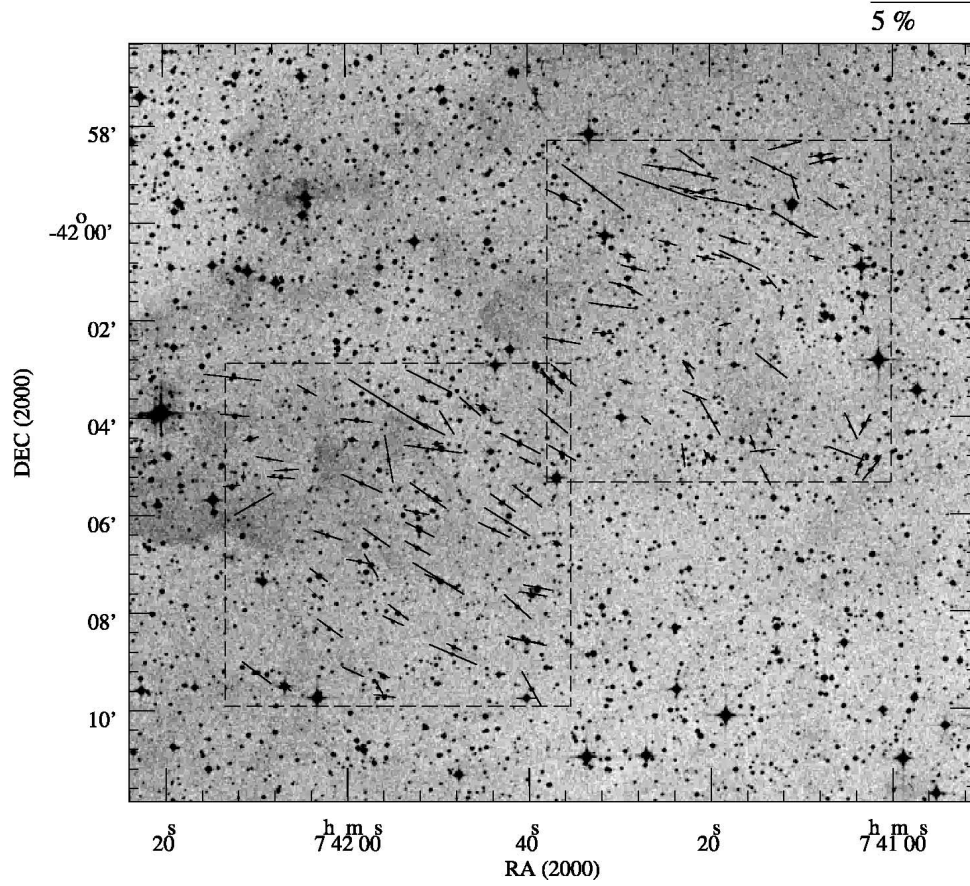


FIG. 10.—Polarization vector map for fields 03 and 02

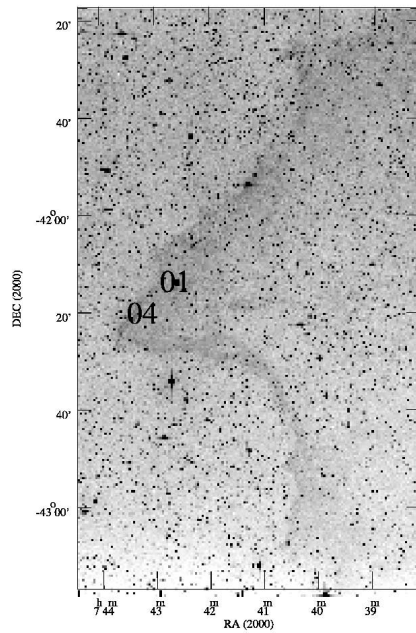
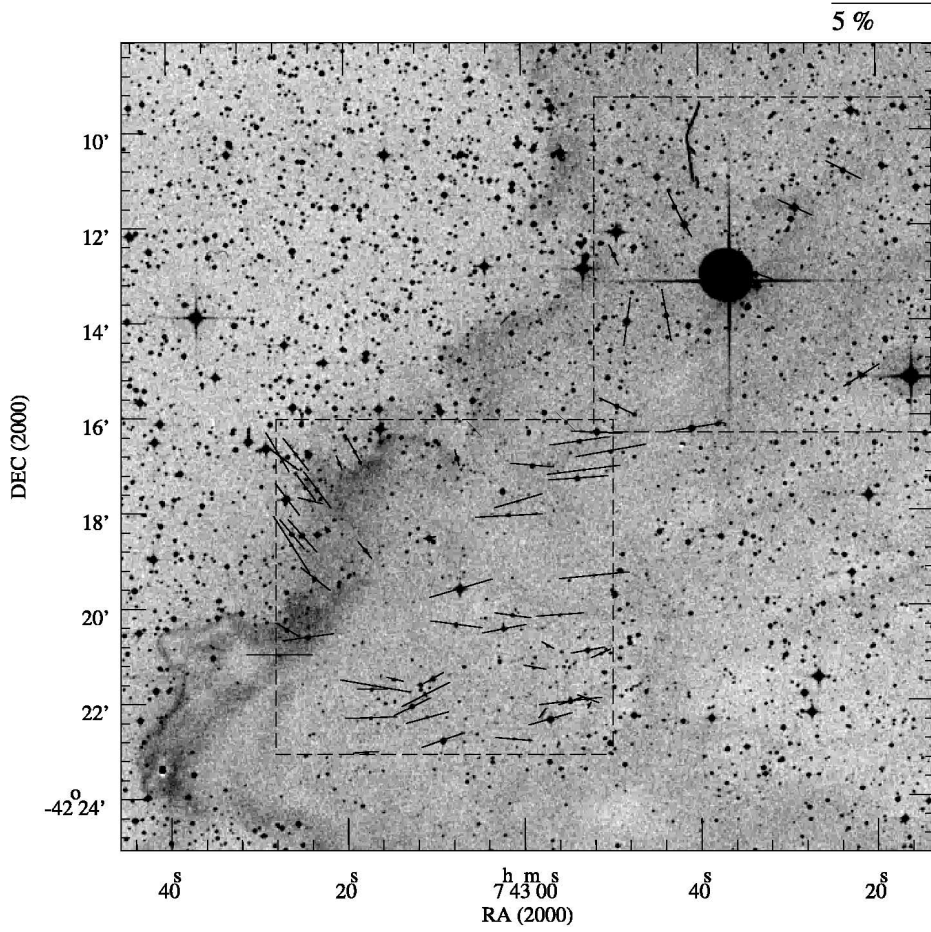


FIG. 11.—Polarization vector map for fields 01 and 04. The brightest star is HD 62542.

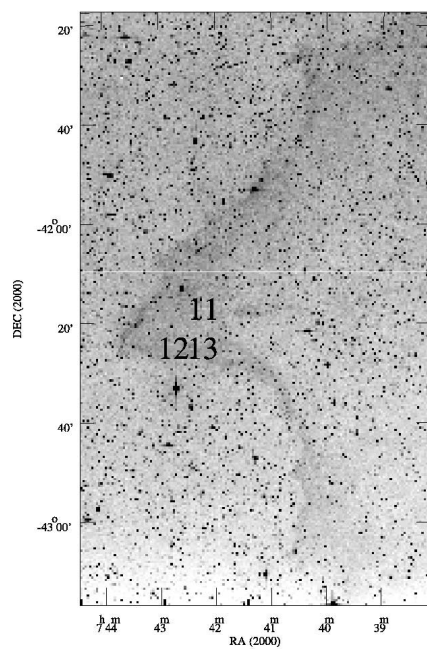
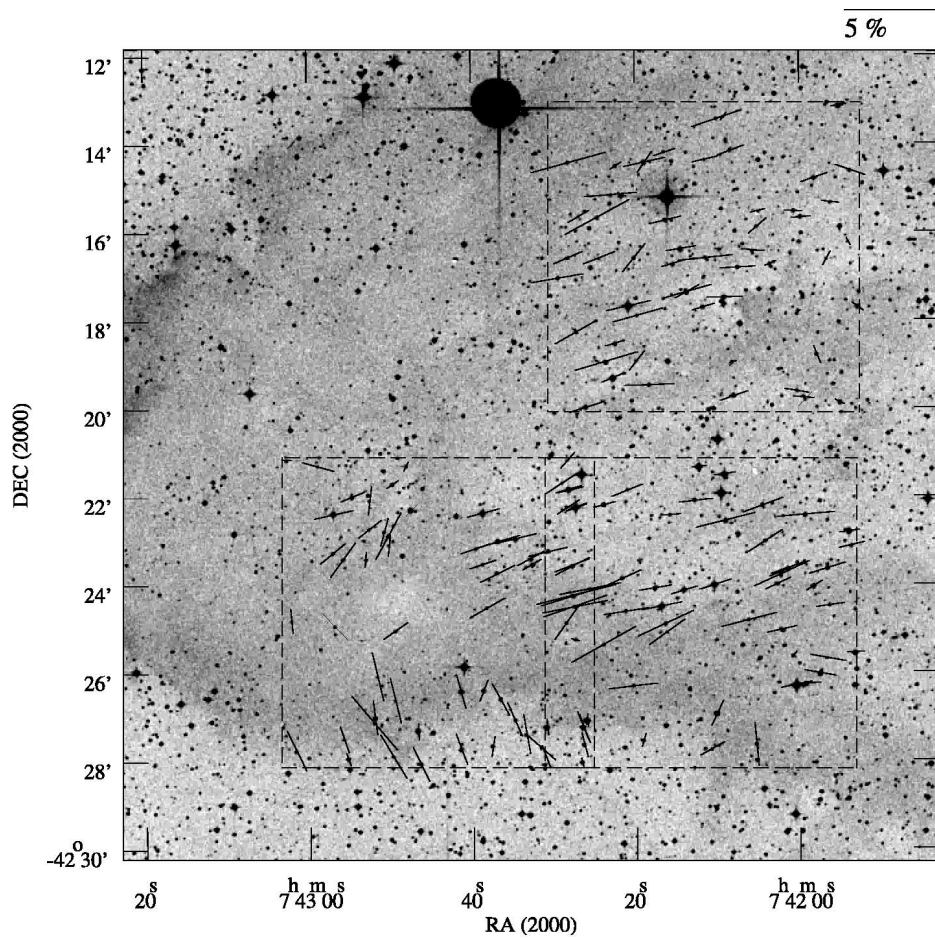


FIG. 12.—Polarization vector map for fields 11, 12, and 13

which can be noticed as the region relatively devoid of stars close to the field center. In fact, it is entirely possible that one is witnessing the result of a continuous twist of the prevailing field direction from northeast to the southern parts of field 12. Looking closely to the pattern of field 13, a transition from parallel to perpendicular orientation with respect to the ridge is also indicated, though the data are more scarce near the ridge.

#### 4.1.7. Fields 13 and 14

In Figure 13 we show the polarization map of fields 13 and 14. The area covers  $20' \times 12'$  ( $2.6 \times 1.6$  pc). The southern border of the ridge is very evident in this image. The pattern of the polarization vectors in field 14 shows a twist across the CCD frame similar to that shown by field 12 discussed above: away from the ridge, the pattern runs more

or less parallel to ridge, and across the ridge, the pattern runs roughly perpendicular to it.

#### 4.1.8. Fields 15 and 16

The polarization map associated with fields 15 and 16 is shown in Figure 14. The picture covers  $12' \times 20'$  ( $1.6 \times 2.6$  pc). These are the southernmost regions of the ridge, for which we have data. Field 15 presents a limited sample of objects but some of them across the ridge have polarization angles parallel to the ridge. Field 16 has a good sample but shows no preferred pattern. We also note that the diffuse emission is not uniform in this area.

## 4.2. Summary and General Comments

The polarization data and maps suggest that the magnetic field lines are often correlated, in more than one way, with

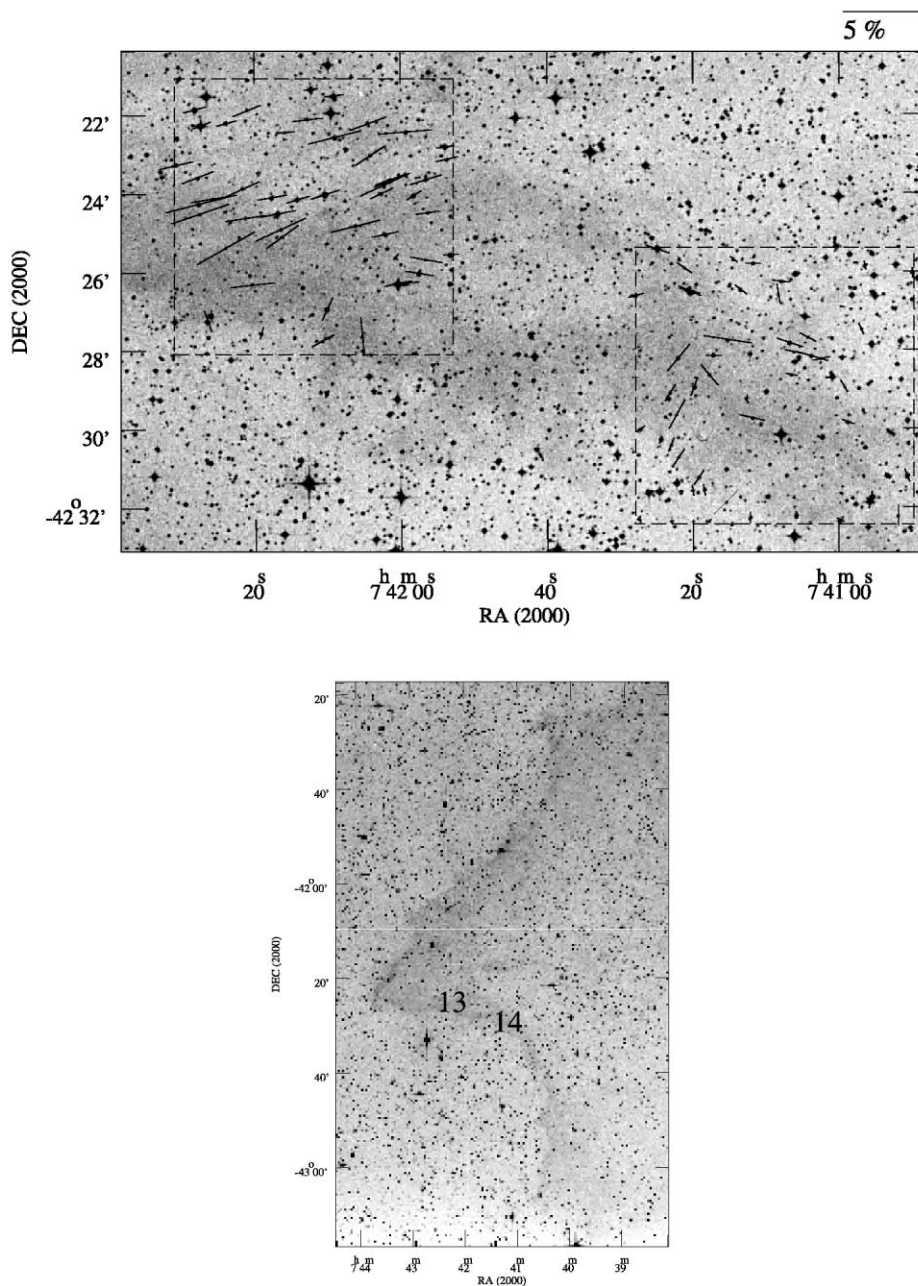


FIG. 13.—Polarization vector map for fields 13 and 14

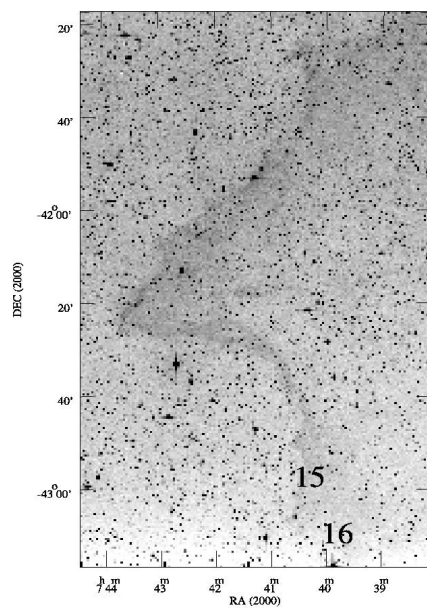
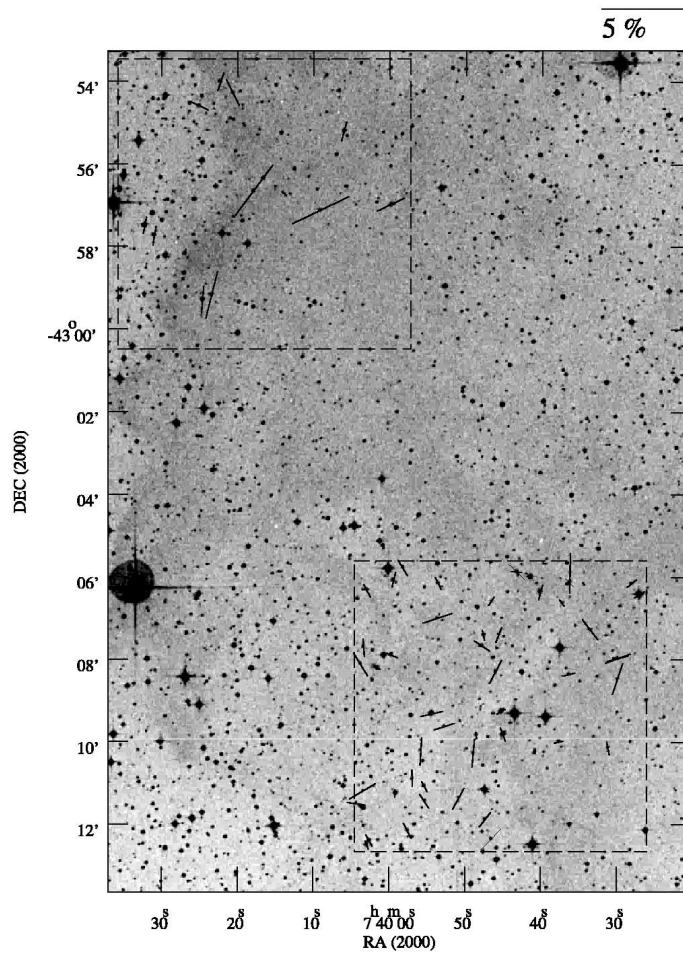


FIG. 14.—Polarization vector map for fields 15 and 16

the morphology of the I/S-front. The best example is the pattern of CCD field 07, where the field lines follow the ridge morphology closely and parallel to it (Figs. 3, 5, and 7).

A second pattern is observed in which the projected field appears to be perpendicular to the ridge, often with a smooth transition to a different geometry within the CCD field in question (e.g., Fig. 12, field 04). A rotation of the magnetic field into the shock is predicted by models of shocks with oblique magnetic fields (Hartquist, Pilipp, & Havnes 1997; Wardle 1998). Another interesting possibility is that the magnetic field lines could be normal to the ridge as the neutral gas is photoionized and expands away toward the ionizing star (R. Reynolds 2000, private communication).

In addition, in either morphology the field lines may at times be coherent over relatively large areas ( $\sim 4$  pc) of the nebula. The best example is fields 05 through 08 (Figs. 7 and 8). Our observations in fact support the fact that the time-scale for grain alignment is shorter than the dynamical time of matter flow throughout the region.

Another finding is that the polarization pattern across some fields seems to follow the flow of gas associated with two condensations within the nebula (fields 02 and 04, Figs. 10 and 11). Mechanical alignment of grains, first suggested by Gold (1952), is able to use a stream of gas to impart angular momentum to the particles normally to the flow direction. Lazarian (1994); Lazarian (1997) has amplified Gold's mechanism to include effects of magnetic field, suprathermal rotation, internal energy dissipation, and the grain-gas drift direction with respect to the magnetic field. In his model Lazarian shows that the grains are aligned (with different efficiencies for oblate and prolate grains) with their longest axis along or perpendicular to the magnetic field depending on whether the flow is directed along or perpendicular to the magnetic field. Oblate particles are more easily aligned for flows normal (i.e., from  $90^\circ$  to  $55^\circ$ ) to the field than along (i.e., within  $55^\circ$  of) the field. Prolate particles are best aligned for flows parallel to the field but they are much more difficult to align than oblate particles.

These ideas can be applied to the observations reported here. The smooth pattern of polarization vectors (such as that displayed by field 07) across large areas implies that there is probably an overall magnetic field close to the IVS ridge. In this case, both the mechanical flow mechanism (as described above) and the Davis & Greenstein (1951) (DG) mechanism are in principle consistent with our data. In the DG scenario, the magnetic field must be generally parallel to the ridge: the grains, which would tend to have their smallest axis aligned with the field, would then produce the observed polarization. In the mechanical flow scenario outlined in the previous paragraph, and since the matter flows are expected to be normal to the shocks, the magnetic field could be either parallel or perpendicular to the ridge. In either case, the smallest axis of the grains would be roughly

parallel to the ridge and again match the observed polarization direction.

The situation is different, however, for the observed pattern *near the condensations*, which shows polarization vectors *along* the associated flow past the condensations. If the direction of the projected magnetic field near such regions were normal to this flow (i.e., still roughly parallel to the ridge), the predicted polarization direction would be normal to the observed direction, as the particles would be spinning with their smallest axis along the field. If the magnetic field were instead along the flow, the flow alignment of the particles' longest axis would be along the field and again provide a polarization direction at odds with the observations. Our data would, however, be consistent with a magnetic field along the flow and with the particles aligned mostly perpendicular to it, as in the traditional DG mechanism.

The more straightforward interpretation of our observations is then that they are consistent with the DG mechanism being operative throughout the region. In this case, the general magnetic field (away from the condensations) would be generally parallel to the ridge. It is in any case clear that these observations of the IVS carry great value as a constraint and diagnostics of potential grain alignment mechanisms.

In a forthcoming paper on the IVS, we will use the catalog to study in detail the histograms within each CCD field in order to estimate the magnetic field strength. We will also correlate the polarization data with extinction across the nebula. This should help understand the alignment mechanism and its efficiency across the IVS in comparison with that of the diffuse ISM.

## 5. CONCLUSIONS

We have employed optical imaging polarimetry to map the magnetic field along the I/S-front associated to the west side of the *IRAS* Vela Shell toward HD 62542. A catalog of polarimetric data for 856 objects with a polarimetric S/N ratio larger than 10 is presented (see Table 2 and Fig. 15, available in the on-line edition of the *Astrophysical Journal Supplement*). The geometry of the polarization vectors shows more than one alignment "type" in relation to the shell morphology. A "parallel alignment" with the border of the I/S-fronts is observed in fields away from the ridge. Across the ridge, a "perpendicular" alignment with respect to the border is often observed. Finally, the geometry of the polarization vectors in parts of the nebula seems to reflect the gas flow past condensations that exist along the shell.

The authors wish to thank the anonymous referee for his careful reading. His several comments and suggestions greatly helped to improve the paper. A. P. is thankful to CAPES and FAPESP for financial support. A. M. M. is thankful to the support of FAPESP and CNPq. Polarimetry at IAG-USP is supported by FAPESP through grant 97/11299-2.

## REFERENCES

- Cardelli, J. A., & Savage, B. D. 1988, *ApJ*, 325, 864  
 Churchwell, E., Winnberg, A., Cardelli, J., Cooper, G., & Suntzeff, N. B. 1996, *ApJ*, 469, 209  
 Clayton, G. C., et al. 1992, *ApJ*, 385, L53  
 Davis, L., & Greenstein, J. L. 1951, *ApJ*, 114, 206  
 Draine, B. T., & McKee, C. F. 1993, *ARA&A*, 31, 373  
 Feitzinger, J. V., & Stüve, J. A. 1984, *A&AS*, 58, 365  
 Gold, T. 1952, *MNRAS*, 112, 215  
 Hartquist, T. W., Pilipp, W., & Havnes, O. 1997, *Ap&SS*, 246, 243  
 Hawarden, T. G., & Brand, P. W. J. L. 1976, *MNRAS*, 175, 19P  
 Jones, R. V., & Spitzer, L. 1967, *ApJ*, 147, 943  
 Jones, T. J. 1996, in *ASP Conf. Ser. 97, Polarimetry of the Interstellar Medium*, ed. W. G. Roberge & D. C. B. Whittet (San Francisco: ASP), 381  
 Lasker, B. M., Sturch, C. R., McLean, B. J., Russell, J. L., Jenkner, H., & Shara, M. M. 1990, *AJ*, 99, 2019

- Lazarian, A. 1994, MNRAS, 268, 713  
———. 1997, ApJ, 483, L296  
———. 2000, in ASP Conf. Ser. 215, Cosmic Evolution and Galaxy Formation: Structure, Interactions and Feedback, ed. J. Franco & E. Terlevich (San Francisco: ASP), 69
- Lazarian, A., Goodman, A. A., & Myers, P. C. 1997, ApJ, 490, L273
- Magalhães, A. M., Benedetti, E., & Roland, E. 1984, PASP, 96, 384
- Magalhães, A. M., Rodrigues, C. V., Margoniner, V. E., & Pereyra, A. 1996, in ASP Conf. Ser. 97, Polarimetry of the Interstellar Medium, ed. W. G. Roberge & D. C. B. Whittet (San Francisco: ASP), 118
- Pereyra, A. 2000, Ph.D. thesis, Univ. São Paulo
- Pilipp, W., & Hartquist, T. W. 1994, MNRAS, 267, 801
- Pilipp, W., Hartquist, T. W., & Havnes, O. 1990, MNRAS, 243, 685
- Redman, M. P., Williams, R. J. R., Dyson, J. E., Hartquist, T. W., & Fernandez, B. R. 1998, A&A, 331, 1099
- Reipurth, B. 1983, A&A, 117, 183
- Reynolds, R. 1976a, ApJ, 203, 151  
———. 1976b, ApJ, 206, 679
- Sahu, M. S. 1992, Ph.D. thesis, Rijksuniversiteit Groningen
- Sandqvist, Aa. 1976, MNRAS, 177, 69P
- Simmons, J. F. L., & Stewart, B. G. 1985, A&A, 142, 100
- Spitzer, L. 1978, Physical Processes in the Interstellar Medium (New York: Wiley), 221
- Troland, T. H., & Heiles, C. H. 1982, ApJ, 260, L19
- Vilas-Boas, J. W. S., Myers, P. C., & Fuller, G. A. 1994, ApJ, 433, 96
- Wardle, M. 1998, MNRAS, 298, 507
- Whittet, D. C. B., Martin, P. G., Fitzpatrick, E. L., & Massa, D. 1993, ApJ, 408, 573
- Williams, R. J. R., Dyson, J. E., & Hartquist, T. W. 2000, MNRAS, 314, 315
- Zealey, W. J., Ninkov, Z., Rice, E., Hartley, M., & Tritton, S. B. 1983, Astrophys. Lett., 23, 119